Electrochemical Investigation of Moisture Byproducts in Molten Calcium Chloride

Rankin Shum[a,b], Marah Fuller[a], Tyler Williams[a], Devin Rappleye[a,z,*]

[a]Department of Chemical Engineering, Brigham Young University, Engineering Building 330, Provo, UT 84602, USA

[b]Current Affiliation: Technology and Innovation, Materion Advanced Materials, 407 N 13th St, Milwaukee, WI 53233, USA, rankin.shum@materion.com

[z]Corresponding author: devin_rappleye@byu.edu

Abstract

Residual water in molten $CaCl_2$ reacts to form different byproducts, such as HCl, which can impact the corrosivity of the salt and efficiency of electrochemical operations, such as electrolytic oxide reduction and electrorefining. The ability to detect and quantify these byproducts electrochemically can provide feedback on the efficacy of vacuum drying and other purification methods, as well as the impact of these byproducts on process operations. An electrochemical signal's association with the production of H_2 is verified and characterized using cyclic voltammetry (CV) and residual gas analysis. CV estimated a 2-electron exchange process associated with H_2 production. CV detected trace quantities of an oxidized species containing hydrogen in the salt on the order of 10 ppm. Different salt handling methods were compared for their impact on the hydrogen electrochemical signal. It was found that 30 minutes of exposure of $CaCl_2$ in a beaker to low-humidity air (<20%) had minimal impact on the H_2 production signal.

Keywords: Molten salts; cyclic voltammetry; hydrogen; calcium chloride

Introduction

Molten chloride salts have potential application in existing and developing industrial technologies, including carbon capture and utilization, thermal energy storage, solar energy, nuclear energy, and liquid metal batteries.[1] Calcium chloride, specifically, is used in actinide metal processing.[2] In addition, due to calcium chloride's high solubility for calcium oxide, it has been a targeted process medium for various metal oxide reduction processes, most notably titanium oxide reduction.[3–7] In these applications, impurities can have a significant impact on corrosion, process efficiency, and product purity. Electrochemical techniques can potentially provide in situ and rapid feedback on the impurity levels and quality of molten chloride salts.[1]

Impurities containing oxygen and hydrogen, such as oxides and hydroxides, are introduced from side reactions occurring during the dehydration of chloride salts. Due to their hygroscopic nature, chloride salts absorb moisture. Calcium chloride is especially hygroscopic and is deliquescent at some of the lowest relative humidities (27-31%) of the chloride salts.[8] Moisture and its byproducts can reduce efficiency and increase corrosion within processes utilizing molten $CaCl_2$ and other chlorides.[9–12] Hence, careful drying of $CaCl_2$ is requisite to minimize undesirable byproducts from interfering with desired electrochemical reactions in molten $CaCl_2$. Various drying procedures have been reported in the literature, some of which dry $CaCl_2$ in air,[13] under vacuum,[9,14,15] under inert gas,[16] under HCl,[17] and under argon initially then under vacuum[18] for varying amounts of time. However, despite careful drying of $CaCl_2$, researchers have reported evidence of residual moisture and/or its byproducts in molten $CaCl_2$ during electrochemical measurements.[9,13–18]

When drying $CaCl_2$ and its hydrates, multiple reactions occur depending upon the temperature and other variables (e.g., partial pressure of water). The discrete decompositions of

the hexa- and tetrahydrate were unobservable in thermogravimetric analysis (TGA) due to their melting points being below the decomposition temperatures resulting in a liquid solution of $CaCl_2$ and H_2O.[19] Based on two TGA studies, the dihydrate is formed slightly below 353 K when the partial pressure of water is ≤5 kPa.[19,20] The dihydrate is reported to fully decompose, as shown below, at 373-443 K under flowing nitrogen depending on heating rate (0.1-10 K/min),[20] and at 423 K if the partial pressure of water is 5 kPa at a heating rate of 0.2 K/min.[19]

$$CaCl_2 \cdot 2H_2O \rightarrow CaCl_2 + 2H_2O_{(g)} \quad (1)$$

However, during drying, moisture can remain trapped in enclosed pores in calcium chloride particles. Additionally, calcium hydroxide and calcium oxide may be present as impurities in the stock $CaCl_2$ and/or formed by the reaction of moisture with calcium chloride.[21]

$$CaCl_2 + 2H_2O_{(g)} \leftrightarrow Ca(OH)_2 + 2HCl_{(g)} \quad (2)$$

$$CaCl_2 + H_2O_{(g)} \leftrightarrow CaO + 2HCl_{(g)} \quad (3)$$

Above 785 K, calcium hydroxide starts to decompose to form water vapor and calcium oxide, even in the presence of $CaCl_2$ in dry atmospheres.[21–24]

$$Ca(OH)_2 \leftrightarrow CaO + H_2O_{(g)} \quad (4)$$

While the electrochemical behavior of oxide ions generated from residual moisture in molten $CaCl_2$ has been extensively investigated,[15,18,22] the fate and behavior of hydrogen from residual moisture has received relatively little attention. Recently, gas bubbles have been observed on molybdenum electrodes with high-speed microscopes.[9,25] When gas bubbles were present, they interacted with Ca and Li-Ca deposits to create precipitates and a metal fog, which resulted in reduced coulombic efficiency. The gas bubbles were assumed to be pure hydrogen

based on increases in current in the potential range of -0.5 to -1.5 V vs. Ag/AgCl(0.5 mol%) with $CaCl_2 \cdot 2H_2O$ additions and measurements of H_2 gas evolution in LiCl-Li_2O-$Li(OH)_2$ melts.[26,27] Natsui et al.[9] postulate that hydrogen is generated from hydrogen ions created from dissociation of water in molten $CaCl_2$, as shown below.

$$H_2O_{(g)} \leftrightarrow 2H^+ + O^{2-} \quad (5)$$

$$2H^+ + 2e^- \leftrightarrow H_{2(g)} \quad (6)$$

The reactions in Eq. 5 and 6 are unconfirmed and other reactions are possible.[28] Hence, more investigation of current signals in the range of -0.5 to -1.5 V vs. Ag/AgCl(0.5 mol%) in molten $CaCl_2$ is needed to clarify the electrochemical processes occurring and their relation to byproducts from moisture. Furthermore, the evolution of H_2 gas needs to be chemically confirmed because the hydroxide ion is proposed to be the source of hydrogen gas in LiCl-Li_2O-LiOH.[26,27] Yet, the hydroxide ion is an unlikely source of hydrogen in molten $CaCl_2$ due to Eq. 4 and the higher melting point of $CaCl_2$ (1045 K). Lastly, the additions of $CaCl_2 \cdot 2H_2O$ in the previous study were large, resulting in indistinct features in the current response and prohibiting the application of voltammetric models to identify properties of the electrochemical reaction.[9]

Hence, this study examines the electrochemical response in molten $CaCl_2$ in the range of -0.5 to -1.5 V vs. Ag/AgCl(0.5 mol %) to: (1) investigate the properties of the associated reaction under dilute conditions; (2) determine the effect, if any, of the drying and handling treatment of $CaCl_2$ on the signal; (3) confirm the chemical identity of the product of the reaction. The electrochemical response and products in molten $CaCl_2$ over the span of -0.5 to -1.5 V vs. Ag/AgCl(0.5 mol%) are interrogated using voltametric techniques and a residual gas analyzer for batches of $CaCl_2$ with different treatments after vacuum drying. The characterization of the

electrochemical response could enable rapid, *in situ* feedback on the quality of the $CaCl_2$ and the hydrogen content. Furthermore, the minimization of this response could decrease corrosion, reduce competing reactions, and increase the reduction efficiency in electrolytic oxide reduction, electrorefining, and other electrochemical processes in molten salts containing $CaCl_2$.

Experimental

Electrochemical Cell.—Electrochemical experiments were performed in a split tube furnace within an argon atmosphere glovebox. Further details on the setup of the glovebox, tube furnace, and gas analyzer were presented elsewhere.[29,30] The salt was contained in alumina crucibles (Advalue Technology, >99.6% Al_2O_3, 40mm OD, 95mm height) which were placed inside the furnace and held at an elevated position within the furnace heating zone. $CaCl_2$ was melted within the furnace at 1113-1133 K. The working electrode (WE) for all experiments was a 1.5mm W rod (Alfa Aesar, 99.95%, 42233) and the counter electrode (CE) was a 3.175mm W rod (Alfa Aesar, 99.95%, 10407). The quasi-reference electrode (QRE) was a 0.5mm W wire (Alfa Aesar, 99.95%, 42233) in all experiments except one where an Ag/AgCl reference electrode (RE) was used (to calibrate the QRE potentials by comparing the Ca deposition potentials). The Ag/AgCl RE was constructed using a closed-one-end alumina tube (AdValue Technology, 4.76 mm ID, 6.35 mm OD, 305 mm height), AgCl (Thermo Scientific Chemicals, 99.997%), dried $CaCl_2 \cdot 2H_2O$ (Thermo Fisher Scientific Chemicals, >99.0%), and 0.5 mm Ag wire (Thermo Scientific Chemicals, 99.9985%). The arrangement of the electrochemical cell is illustrated in Figure 1. A potentiostat (Autolab, PGSTAT302N) and the accompanying software (NOVA 2.1) was used to conduct and analyze electrochemical measurements.

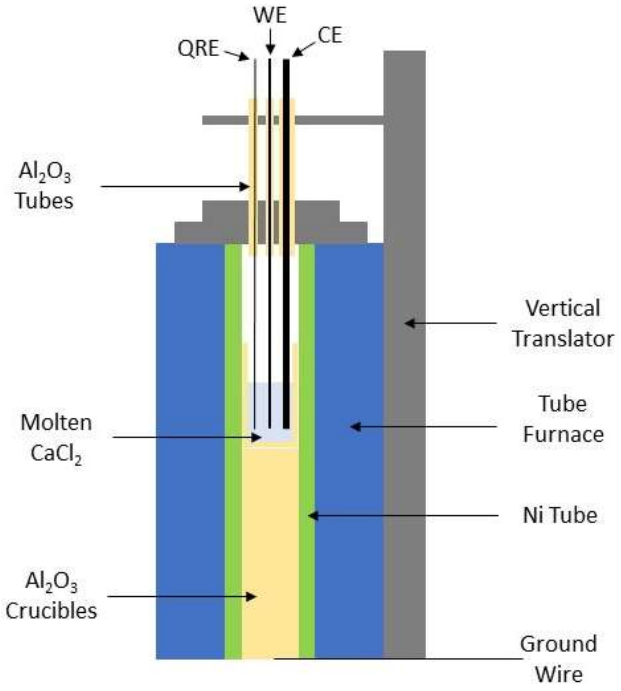

Figure 1. Illustration of electrochemical cell setup.

Materials Preparation.—*Alumina Crucibles.*—Some of the crucibles were reused after prior experiments. Before reuse, the crucibles were first immersed in water at low heat to dissolve remaining salt contaminants and then immersed in aqua regia solution—5 vol% 1:3 HNO_3 (Fisher Chemical, 69-70% w/w, A200-500) to HCl (Fisher Chemical, 36.5-38% w/w, A144-500) in distilled water. They were boiled in this solution for at least 30 minutes, and then rinsed with water. New and reused ceramics were dried for 6 or more hours in a vacuum furnace (Across International Vacuum, Model AT32e), after which they were transferred to the glovebox and dried for an additional 2 hours at 1173 K in the tube furnace.

Calcium Chloride Salt*.*—$CaCl_2$ for electrochemical experiments was prepared using three different methods: controlled exposure (CEP), direct transfer (DT), and pre-melted (PM). For all three methods, anhydrous $CaCl_2$ was produced via thermal dehydration of $CaCl_2 \cdot 2H_2O$

(>99.0%, Thermo Fisher Scientific Chemicals, Inc.). The composition of the $CaCl_2 \cdot 2H_2O$ reported in the certificate of analysis is shown in Table 1.

Table 1. Composition of calcium chloride dihydrate

Component	**Concentration**
Calcium chloride dihydrate	99.86%
Insoluble Matter	0.0044 %
Sulfate	< 0.01 %
Ammonium	< 0.005 %
Barium	< 0.005 %
Heavy metals (as Pb)	< 5 ppm
Iron	< 5 ppm
Magnesium	0.0021 %
Potassium	0.0019 %
Sodium	0.0067 %
Strontium	0.0001 %
Oxidizing substances (as NO_3)	< 0.003 %

The dehydration occurred within a vacuum oven (Across International Vacuum, Model AT32e). First, the $CaCl_2 \cdot 2H_2O$ was placed in a glass dish and then covered with an aluminum plate with holes in it to prevent rust from falling into the sample. The oven was then placed under vacuum, reaching less than 2 kPa absolute pressure. The following drying procedure was followed: 5 hours at 303 K, 11 hours at 363 K, 8 hours at 393 K, and at least 48 hours at 503 K. Each temperature step was selected based on thermogravimetric analysis from previous studies (see discussion in the Introduction).[19,20]

After drying, the vacuum oven was backfilled with ultra-high-purity (UHP) nitrogen gas. For the CEP preparation method, the dried salt in a borosilicate 400 mL beaker was allowed to cool to room temperature and removed from the drying oven, immediately placed on a scale in the lab, and exposed to ambient air for 30 minutes. Following the 30 minutes of exposure, the $CaCl_2$ was transferred to the argon atmosphere glovebox (<1 ppm O_2 and H_2O) in less than 1

minute. $CaCl_2$ salt prepared with the DT method was transferred immediately to the glovebox from the vacuum oven, with less than 1 minute of total exposure to air. Lastly, the PM salt followed the DT method, after which it was melted and cooled back to room temperature within the tube furnace in the glovebox.

$CaCl_2 \cdot 2H_2O$ was added to DT-treated $CaCl_2$ while molten for one experiment. For additions while molten, the mass of the $CaCl_2 \cdot 2H_2O$ was measured and then inserted into the alumina crucible within the furnace. The first and second additions were ≤0.259 g and ≤0.266 g, respectively. Due to small spills and vaporization, the amount of water introduced to and reacted with molten $CaCl_2$ could not be determined.

Electrochemical Methods.—Cyclic voltammetry (CV) and chronoamperometry (CA) electrochemical tests were performed in the molten $CaCl_2$. In CV, scan rates were varied from 0.1 to 1.0 V s^{-1} with a digital staircase potential step of 1 mV. At least four scans were performed at each scan rate in each experiment to ensure reproducibility.

The resistance compensation value for each salt was determined by first looking at the potential where the reduction current crossed -0.0052 A cm^{-2}. This potential was used in a current-interrupt test to estimate the value of the uncompensated resistance. Lastly, this estimate was inputted into a positive feedback test and adjusted, if needed, until oscillations were contained to within 1 ms after a potential pulse.

Titrations.—Back titrations were performed to measure hydroxide and oxide content in the salt, as described in the subsequent paragraph, and thus correlate those values to the salt's preparation method. CEP- and DT-treated salts were analyzed using back titrations prior to

electrochemical measurements. PM salts were not titrated between the pre-melting and electrochemical tests.

Each sample's mass was measured within the glovebox, transferred out of the glovebox, dissolved in purified water (Thermo Fisher Scientific Chemicals, Inc., Model D4631, ≥17 MΩ-cm), and then titrated using a Metrohm auto-titrator (916 Ti-Touch). During each titration, an excess of 0.1 M HCl was added which neutralized the OH^- ions from $Ca(OH)_2$ and then acidified the solution. 0.1 M NaOH was then added, neutralizing the excess HCl and reaching an equivalence point (i.e., inflection point on the pH vs. volume of NaOH added curve). The volume of 0.1 M NaOH added to reach the equivalence point indicates the volume of excess 0.1 M HCl that was present. The excess volume of 0.1 M HCl is subtracted from the volume of 0.1 M HCl added to obtain the volume of 0.1 M HCl which reacted with $Ca(OH)_2$. Using the volume of 0.1 M HCl reacted and the stoichiometry in Eq. 7, the amount of $Ca(OH)_2$ present in the sample is calculated.

$$Ca(OH)_2 + 2HCl \leftrightarrow CaCl_2 + 2H_2O \quad (7)$$

A similar procedure was performed following the electrochemical experiments of each salt sample. However, CaO was presumed to be present in the sample instead of $Ca(OH)_2$ due to known reactions in Eq. 3 and 4. CaO reacts in water to form $Ca(OH)_2$ (i.e., $CaO + H_2O \leftrightarrow Ca(OH)_2$)[31] and the calculated $Ca(OH)_2$ content of dissolved sample was inferred to be the CaO content of melted $CaCl_2$ prior to dissolution.

Gas Analyzer.—In some experiments, the exhaust gas from the electrochemical cell was analyzed to identify evolved gases during heating of the salt and from electrochemical reactions. For these experiments, the Ni tube in Figure 1 was replaced with a one-end-closed Ni pipe

welded to a Ni flange. A custom-made Ni flange lid with sealed electrode feedthroughs and gas inlet and outlet was bolted to the flange welded to the Ni tube with a graphite foil gasket in between to seal the Ni chamber. More details on the Ni chamber can be found elsewhere.[30] The outlet of the sealed electrochemical cell was connected to a Pfieffer Vacuum residual gas analyzer (Omnistar 350).

A complete seal could not be achieved with a Ag/AgCl RE. Hence, a QRE was used in this experiment. To seal the QRE, a W wire was pierced through a Viton stopper, which was secured inside of a compression fitting in the lid CV was performed to determine the potential of the hypothesized hydrogen evolution signal. Potentials of -0.5, -0.8 and -0.9 V vs. W QRE were applied to the WE and a sweep gas of dry argon (<1 ppm H_2O, <1 ppm O_2) flowed through the electrochemical cell and to the gas analyzer. The stability of the QRE during electrolysis was verified by comparing CV scans before and after 5 minutes of electrolysis and observing no shift in Ca deposition potential. Similar observations of the stability of W QRE were observed by Dring et al.[16]

During electrolysis, the gas analyzer sampled the signal at 2 atomic mass units (AMU) for H_2 to determine if the signal rises above background intensity ($2\text{-}2.5 \times 10^{-12}$). After the gas analyzer began sampling the sweep gas from the electrochemical cell for 20-30 seconds, one of the potentials was applied to see if the signal at 2 AMU would rise above background.

Experimental Outline.—Table 2 below outlines the experiments that were performed with their respective identification number, preparation method, working electrode area, temperature, and compensated resistance. Each experiment represents one day of testing with the same salt, but many different electrochemical tests (CV, SWV, etc.) were performed on that same day.

Table 2. Experiment reference table showing properties of each experiment, including salt preparation method, WE area, temperature, and compensated resistance.

Experiment No.	Preparation Method	WE Area / cm^2	Temperature / K	Compensated Resistance / mΩ
1	CEP	0.891	1120	120
2	CEP	1.14	1131	185
3	DT	1.04	1126	110
4	DT	0.891	1123	100
5	DT[1]	0.891	1126	120
6	PM	0.235	1125	100
7[2]	CEP	---	1131	300
[1]Added ≤0.259 g, then ≤0.266 g $CaCl_2 \cdot 2H_2O$ to molten $CaCl_2$, [2]Ag/AgCl RE used				

Results

Chemical Analysis of Salt.—During the CEP preparation process, the initial mass of the salt was measured after vacuum drying. The mass was then monitored at five-minute intervals over 30 minutes while exposing the dried salt to air to quantify the absorption of moisture from the air into the salt (see Figure S1 and Table S1 in Supplementary Material). The ambient temperature, pressure, and humidity were recorded when exposing batches, A, B , and C to air in the laboratory. The salt mass generally increased linearly over the 30 minutes. For batches A, B, and C, the mass decreased slightly (≤22 mg) or stayed the same in the first five minutes, after which it increases linearly. Table 3 shows the percentage of mass gain over the 30 minutes of exposure for the five batches of CEP salt that were prepared on different days.

Table 3. Conditions and percentage of mass gain of CEP batches of $CaCl_2$. (n.m. = not measured)

Batch	Ambient Temperature /K	Ambient Pressure / kPa	Relative Humidity / %	Initial Mass / g	Change in Mass / %
A	296.5	85.5	17.3	147.70	0.0014
B	300.1	85.1	15.1	147.21	0.0088
C	297.8	85.6	18.5	146.89	0.044
D	n.m.	n.m.	n.m.	146.71	0.065
E	n.m.	n.m.	n.m.	136.02	0.076

Back titrations were performed on salt samples dissolved in purified water to measure the amount of hydroxide (OH^-) present in the salt solution. Based on these measurements, the $Ca(OH)_2$ and CaO content were determined as discussed in the Titrations subsection of the Experimental section. Table 4 reports the mass of salt dissolved in purified water and the amount of OH^- (in moles) measured. During vacuum drying, $Ca(OH)_2$ is assumed to form via the reaction shown in Eq. 2, since drying occurs below the observed thermal decomposition temperature of $Ca(OH)_2$ in its pure form and when mixed with $CaCl_2$. [22–24] The salt mass and measured amounts of OH^- reported in Table 4 after vacuum drying and prior to electrochemical tests (i.e., melting) were used to calculate the presumed $Ca(OH)_2$ content in ppm by moles (ppm) and OH^- by weight (ppmw) using Eq. 8 and 9, respectively,

$$ppm = \frac{N_{Ca(OH)_2}}{\left[\frac{m_s - N_{Ca(OH)_2} \cdot 74.078\ g/mol}{110.98\ g/mol} + N_{Ca(OH)_2}\right]} \times 10^6 \quad (8)$$

$$ppmw = (N_{OH^-} \cdot 17.007\ g/mol)/m_s \times 10^6, \quad (9)$$

where m_s is the sample mass, N_{OH^-} is the measured moles of OH^-, and $N_{Ca(OH)_2}$ is moles of $Ca(OH)_2$ (i.e., $N_{Ca(OH)_2} = 0.5N_{OH^-}$). When the salt is melted to perform electrochemical tests, CaO is assumed to form by the reactions shown in Eq. 3 and 4, as $CaCl_2$ melts above the thermal decomposition

temperature of $Ca(OH)_2$ and hydrolysis of $CaCl_2$ above 1113 K in low moisture atmospheres favors CaO formation.[21–24] Titration measurements after electrochemical tests were used to calculate presumed CaO content in ppm and O^{2-} ppmw using Eq. 8 and 9, respectively, where N_{OH^-}, $N_{Ca(OH)_2}$, 74.078 g/mol, and 17.007 g/mol are substituted with $N_{O^{2-}}$, N_{CaO}, 56.08 g/mol, and 15.999 g/mol, respectively. Recall from the Titration subsection that $CaO + H_2O \leftrightarrow Ca(OH)_2$ (i.e., $N_{O^{2-}} = N_{CaO} = 0.5N_{OH^-}$). Hence, in Table 4, the presumed $Ca(OH)_2$ content of samples from vacuum dried salts and the presumed CaO content of melted salts are presented. The experiment number and drying procedure (i.e., CEP, DT, or PM) are also included for reference (see Calcium Chloride Salt and Experimental Outline subsections in Experimental section).

Table 4. Calculated hydroxide and oxide contents based on back titrations (n.m. = not measured).

Experiment No.	After Vacuum Drying				After Melting			
	Sample Mass / g	Measured OH^- / 10^{-5} mol	$Ca(OH)_2$ Content / ppm	OH^- Content / ppmw	Sample Mass / g	Measured OH^- / 10^{-5} mol	CaO Content/ ppm	O^{2-} Content / ppmw
1 (CEP)	40.019	8.486	117.7	36.06	34.857	8.394	133.6	19.26
3 (DT)	39.540	2.386	33.48	10.26	n.m.	n.m.	n.m.	n.m.
7 (CEP)	n.m.	n.m.	n.m.	n.m.	0.9185	5.550	3347	483.4

Titrations measurements were not performed for experiment 2. For experiments 4-6, accurate OH^- amounts were unable to be determined. Too little HCl was added. Hence, the solution was not sufficiently acidified causing the titrator to add NaOH indefinitely as an equivalence point was never reached. Since there was no equivalence point, an accurate measure of the OH^- content was not possible.

Off-gassing was monitored with the gas analyzer during the heating and melting process of $CaCl_2$, which was prepared using the CEP method (Batch E). Following standard mass

spectrometry practice, raw signals were normalized by the largest signal (i.e., 40 m/z representing Ar). These normalized signals are known as relative abundances, but they do not convey information regarding the concentration of the gas. As seen in Figure 2, HCl (36 m/z) and H_2O (18 m/z) were detected consistently below and at the operating temperature. Due to the gas analyzer being outside of the glovebox, it took several minutes for the gases to travel through a couple meters of tubing to the gas analyzer. Indeed, the spike in all three species at 700 min likely corresponds to when the salt melted, which occurred around 690 min. With the ~10-minute lag accounted for, H_2 (2 m/z) likely started to evolve when the salt was at ~650 K. H_2 could be the product of the reaction of HCl with the Ni reactor chamber to form $NiCl_2$. Reaction of Ni with HCl gas is reported at and above 623 K.[32,33] Nevertheless, the detection of both HCl and H_2O gases indicates that both are possible sources of hydrogen ions in molten $CaCl_2$.

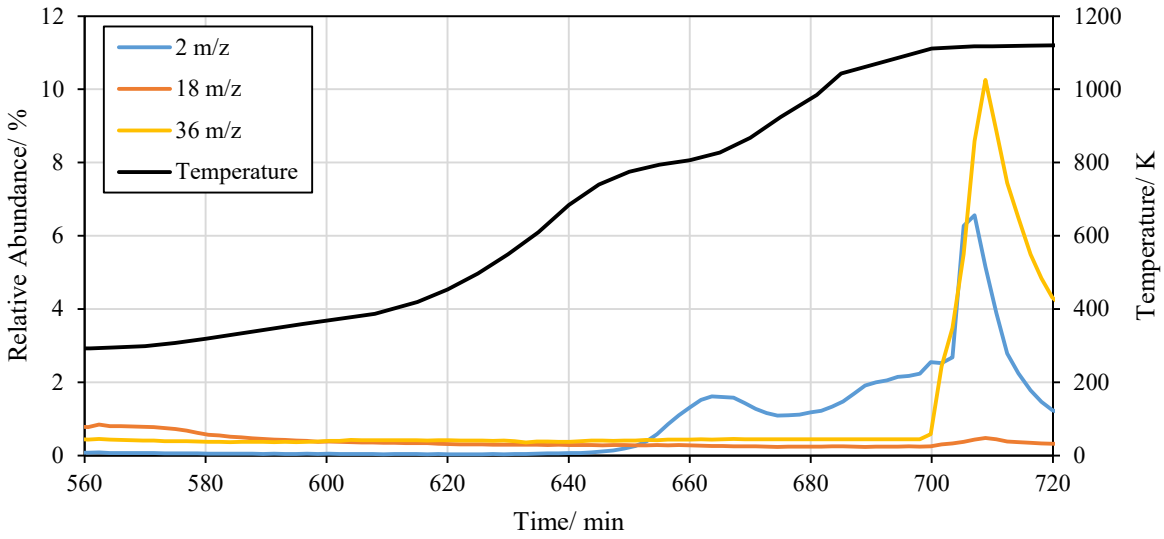

Figure 2. Gas analyzer data taken as $CaCl_2$ (m.p. = 1045 K) was heated.

Cyclic Voltammetry.—A CV response for $CaCl_2$ is shown in Figure 3. The scan range of choice was -1.15 to 1.2 V vs. W QRE. Expanding the range further left or right would lead to

sharp decreases and increases in current, respectively. This range was used to increase visibility of intermediate peaks.

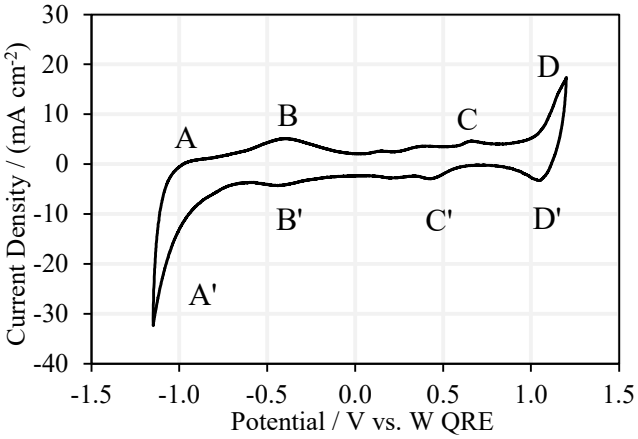

Figure 3. Cyclic voltammogram from experiment 3 at 300 mV s^{-1} (WE: 1.5 mm W rod, CE: 3.175 mm W rod, RE: 0.5 mm W wire).

In Figure 3, the peaks of several electrochemical reactions are visible. A/A' signals correspond to the oxidation of Ca metal/reduction of Ca^{2+}. B/B' are unknown oxidation/reduction peaks, hypothesized to be related to hydrogen by Natsui et al.[9] C/C' are the oxidation of W/reduction of $CaWO_4$.[15] D/D' signals are attributed to the O^{2-}/O_2 redox couple due to the proximity of the O^{2-}/O_2 standard potential of 2.43 V vs. Ca^{2+}/Ca.[15,16,34] In this study, the B/B' peaks were investigated to elucidate the electrochemical reaction occurring in the range of -0.5 to -1.5 V vs. Ag/AgCl (0.5 mol%).

The B/B' peaks were compared within each type of salt (CEP, DT, and PM). Figure 4 shows the overlaid CV responses for experiments 1, 3, and 6. Due to the use of a QRE, the reference potential shifted slightly between experiments. For easier comparison, the potentials in Figure 4 were shifted by 0, -0.2, and -0.9 V for experiments 1, 3, and 6, respectively, to align the electrochemical windows. An approximate calibration to the Ag/AgCl RE scale is provided in

Figure 4 by overlaying measurements in molten $CaCl_2$ from experiment 7 where an Ag/AgCl RE was used. The x-axis at the top of the plot was adjusted until the Ca deposition in experiment 1 and 7 aligned since the salts in both experiments were handled in the same manner (i.e., CEP). Hence, the adjusted potential is approximately 0.25 V vs. Ag/AgCl (6 mol%).

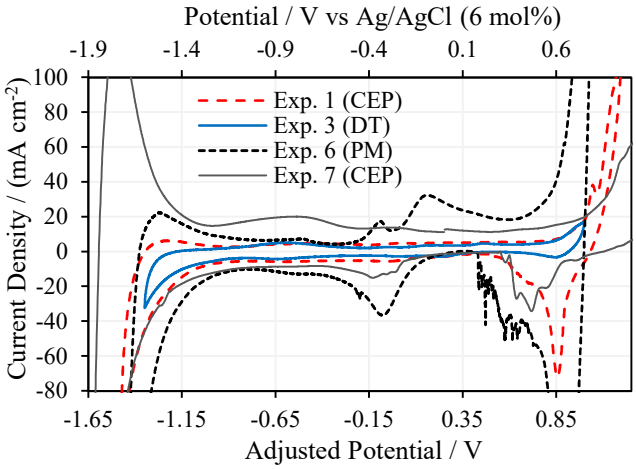

Figure 4. Overlaid CV responses for experiments 1, 3, 6, and 7 at 300 mV s^{-1} where the bottom x-axis reports potentials for experiments 1, 3, and 6 (WE: 1.5 mm W rod, CE: 3.175 mm W rod, RE: 0.5 mm W wire) and the top x-axis reports potentials for experiment 7 (WE: 1.5 mm W rod, CE: 3.175 mm W rod, RE: Ag/AgCl [6 mol%]).

It is difficult to compare the size of B/B' peaks for the three experiments in Figure 4. The baseline for experiment 6 (PM) is much larger than for experiment 1 (CEP) and experiment 3 (DT). On the other hand, the CV responses for experiments 1 and 3 are similar with more pronounced B/B' peaks for experiment 3.

To better understand and characterize peaks B/B', CV scans were performed in the potential range in which peaks B/B' were observed in wider scans presented in Figure 4. Figure

5 shows partial scans overlaid for experiments 1, 3, and 6. The peaks in Figure 5 occur over about -0.2 to -0.7 V based on the adjusted potential. Using the approximate conversion determined from Figure 4, -0.2 to -0.7 V converts to -0.45 to -0.95 V vs. Ag/AgCl (6 mol%). Using the Nernst equation to adjust from 6 mol% AgCl in this work to 0.5 mol% AgCl used by Natsui et al.[9] results in a shift of -0.24 V (RT/F×ln[0.005/0.06]) at 1131 K, which results in a potential range of -0.79 to -1.2 V vs. Ag/AgCl (0.5 mol%) for peaks B/B'. This range lies within the potential range of -0.5 to -1.5 V vs. Ag/AgCl(0.5 mol%) for the current increase with $CaCl_2 \cdot 2H_2O$ additions observed by Natsui et al.[9]

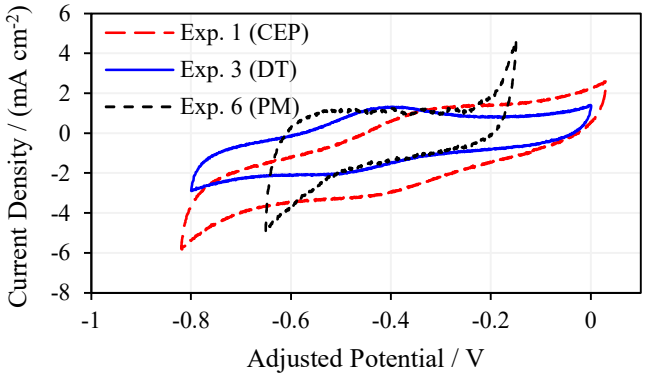

Figure 5. CV responses in B/B' potential range for experiments 1, 3, and 6 at 300 mV s^{-1} (WE: 1.5 mm W rod, CE: 3.175 mm W rod, RE: 0.5 mm W wire). Potentials were adjusted based on alignment of the electrochemical window for easier comparison.

In the CV response of experiment 6, there is effectively no B/B' peak. This is surprising since there are some peaks that appear in the same potential region (-0.3 to -0.7 V) in Figure 3. The peaks in the -0.3 to -0.7 V region in Figure 4 for experiment 6 may be dependent upon the reaction associated with the peaks around 0 V. When the upper limit of the partial scan in PM salt was extended to above -0.1 V at a scan rate of 1 V s^{-1}, the peaks in the -0.3 to -0.7 V range reappeared. In the DT and CEP salts, the peaks in the -0.3 to -0.7 V region still appear in the

partial scan in Figure 5. Experiments 1 and 3 have similar B' peak sizes, with peak heights of 0.544 mA and 1.11 mA, respectively, with background current subtracted. The similar peak heights could be explained by the loss of moisture from CEP salt batches while heating the salt in the furnace and during the transfer into the glovebox, which includes vacuum cycling the antechamber. It was observed for a CEP salt batch that the salt mass decreased by half the amount of mass gained during exposure to air when the salt batch was weighed after transferring into the glovebox. Regardless of the cause, the CEP procedure did not seem to significantly affect peak B'.

The electrochemical behavior of B/B' was studied by varying scan rates between 0.1 V s^{-1} and 1.0 V s^{-1}. Figure 6 below shows the overlaid CV responses of several scan rates. As the scan rate increases, the size of the reduction and oxidation peaks increases. A reversible reaction under semi-infinite linear diffusion control should have a linear relationship between peak height and square root of scan rate and no correlation (i.e., independence) between peak potential and natural log of scan rate. Figure 7 shows the plots of the B' peak height and potential. There is a clear linear trend between peak height and square root of scan rate for each experiment, except at 0.7 V s^{-1} in experiment 1, which seems to be an outlier. The linearity of peak height and square root of scan rate and the independence of peak potential and scan rate for experiments 1-4 provide evidence that the reduction reaction associated with B' is electrochemically reversible and diffusion controlled up to at least 1 V s^{-1}.

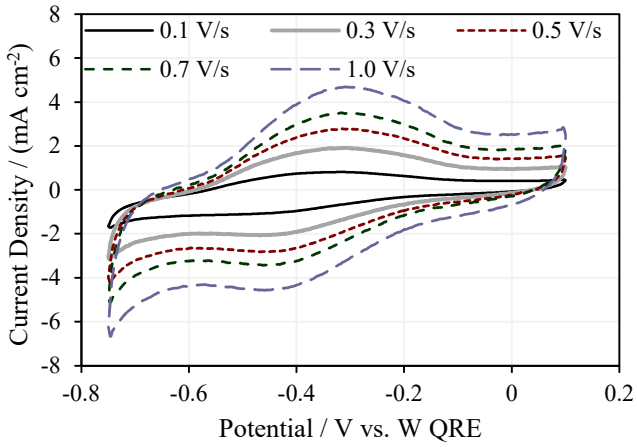

Figure 6. Current density vs. potential for various scan rates in experiment 3, focused on peaks B/B' (WE: 1.5 mm W rod, CE: 3.175 mm W rod, RE: 0.5 mm W wire).

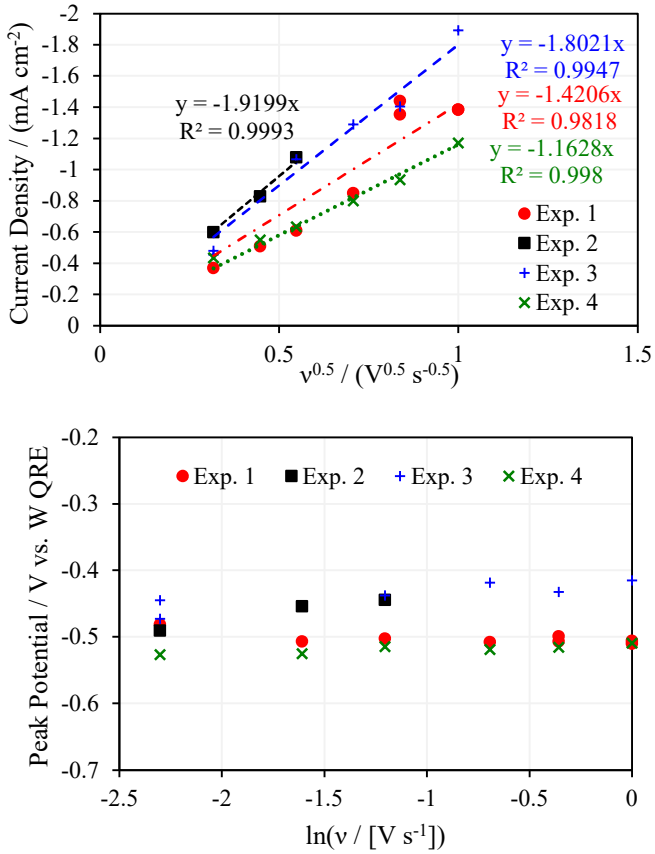

Figure 7. Peak height versus square root of scan rate (top) and peak potential versus natural logarithm of scan rate (bottom) for experiments 1-4.

The shape of the CV curves in Figure 6 takes on the broader shape characteristic of soluble-soluble reactions (i.e., Randels-Ševčik theory),[35–37] rather than the sharper peaks characteristic of soluble-insoluble reactions.[1,38] Indeed, the background-corrected curves in Figure 6 match well the currents tabulated for a reversible, soluble-soluble reaction [36] with exception of the tail of the peak which occasionally decayed more rapidly than predicted by diffusion only models (i.e., Randels-Sevčik theory), as shown in Figure 8.

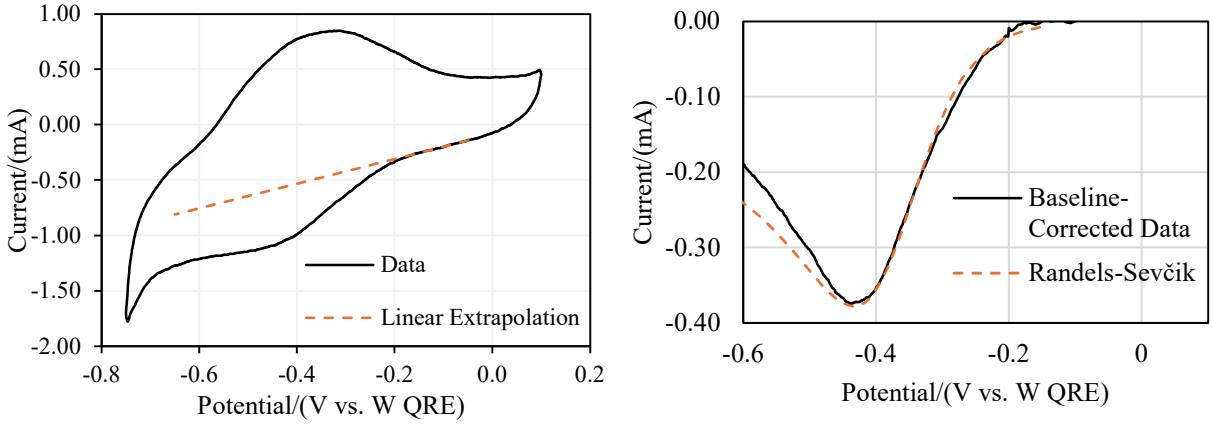

Figure 8. Left: CV response for experiment 3 at 100 mV s^{-1} with linearly extrapolated baseline (WE: 1.5 mm W rod, CE: 3.175 mm W rod, RE: 0.5 mm W wire) . Right: Best fits of baseline-corrected response to peak shape predicted Randels-Ševčik theory ($E_{1/2}$ = -0.38 V, $D_o^{1/2}C_o$ = 3.4 × 10^{-9} mol cm^{-2} $s^{-0.5}$)

The left plot in Figure 8 illustrates the extrapolated baseline current used for background correction. The baseline had to be extrapolated since comparing to a "blank" melt was not an option. These melts were the highest purity achievable in our laboratory and the analyte (i.e. impurity) was dilute (~10^{-6} mol cm^3, if D_o = ~10^{-5} cm^2 s^{-1}). When linearly extrapolating the current at the base of the peak, the corrected current in the right plot closely matches the tabulated values for a reversible, soluble-soluble (i.e., Randles-Sevčik) peak until shortly after

the peak resulting in a root-mean-squared error (RMSE) of 0.021. Hence, at the conditions tested, the product of the reaction correlated with the B' peak may initially have slight solubility in molten $CaCl_2$.

To interpret this result, a brief review of classical nucleation theory for gas bubble formation is needed.[37,39] Initially, gases are produced at an electrode, dissolve into solution, and diffuse away from the electrode. As more gas is accumulated near the electrode, the solubility of the gas in the solution near the electrode is exceeded. When the gas solubility is sufficiently exceeded, gas bubbles begin to form on the electrode. Indeed, Lantelme et al.[40] observed the dynamics of dissolution, diffusion, and bubble formation of Cl_2 gas in molten LiCl-KCl. Furthermore, H_2 has been reported to be soluble in molten salts: FLiBe eutectic (4.84×10^{-8} mol cm^{-3} atm^{-1} at 873 K)[41] and FLiNaK eutectic (1.62×10^{-6} mol cm^{-3} atm^{-1} at 973 K).[42] Hence, it is reasonable that H_2 may have some slight solubility in molten $CaCl_2$ as well. Hence, classical nuclear theory offers a plausible explanation of the results in Figure 8. Initially, reversible, soluble-soluble behavior (i.e., Randels-Ševčik) behavior is observed. However, as more product forms, the solubility of product could be exceeded at the surface of the electrode. Absorbed product and/or gas bubbles may nucleate and begin to block parts of the electrode resulting in a faster current decay than predicted from the depletion of the diffusion layer.

The hydrogen evolution reaction (HER) at high H^+ concentrations (e.g., aqueous solutions) manifest adsorption peaks. However, as noted by Bard et al. [37], "the HER at low H^+ concentrations closely approaches the Nernstian response, implying that each intermediate step is microscopically reversible." This corroborates with our observations of reversible CV peak behavior in Figures 7 and 8. Furthermore, Bard et al. [37] stated that "when [the reduced product] is weakly absorbed, the cathodic current on the forward scan in CV is only slightly perturbed,

while the anodic current on reversal is enhanced." Hence, the absolute value of the ratio of the anodic (reverse) peak current to the cathodic (forward) peak current (i.e. reversal ratio) increases with scan rate. Indeed, reversal ratios for that data in Figure 6 increase from 1.5 at 0.1 V/s to 2 at 1.0 V/s when background corrected (0.77 to 1 with background). Hence, it appears that the reaction behaves reversibly with minor perturbations due to a weakly absorbed reduced product.

With the data in Figures 6-8 exhibiting trends charateristic of reversibile, soluble-soluble behavior, the number of electrons exchanged in the B' reduction reaction can be determined. Using the absolute value of the difference in the peak potential (E_p) and half peak potential ($E_{p/2}$) for a soluble-soluble, reversible reaction, the number of electrons exchanged in the reaction can be estimated with Eq. 10.

$$\Delta E_{p/2} = \left|E_p - E_{p/2}\right| = 2.2\frac{RT}{nF} \tag{10}$$

The $\Delta E_{p/2}$ was determined for the B' peak using the peak fitting operation in NOVA 2.1 after correcting for background current. The resulting values of $\Delta E_{p/2}$ are plotted in Figure 9. Using the values in Figure 9, the number of electrons transferred for the B' reaction were estimated using Eq. 10. These estimates are displayed in Table 5. The average number of electrons exchanged with a 95% confidence interval using a student's t-test is $n = 1.95 \pm 0.17$.

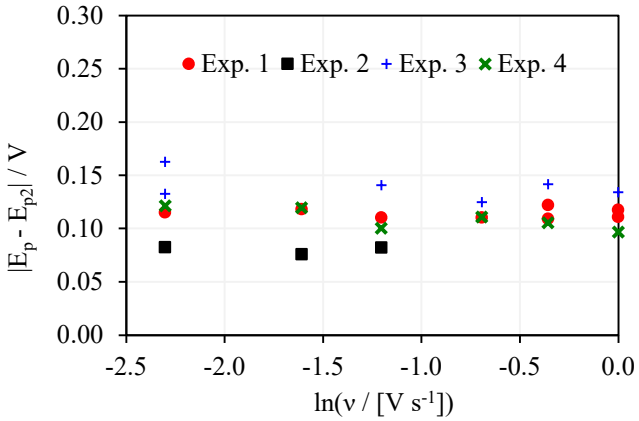

Figure 9. Absolute value of difference in peak potential and half peak potential versus natural logarithm of scan rate for experiments 1-4.

Table 5. Estimated number of electrons from cyclic voltammograms for experiments 1-4.

Scan Rate (V/s)	Number of Electrons Exchanged, *n*			
	Exp. 1	**Exp. 2**	**Exp. 3**	**Exp. 4**
0.1	1.84	2.61	1.61	1.76
0.2	1.80	2.83	---	1.78
0.3	1.92	2.61	1.52	2.12
0.5	1.93	---	1.71	1.92
0.7	1.74	---	1.51	2.02
1	1.91	---	1.59	2.20

Based on the CV data, the overall redox process associated with peak B' involves two electrons. In addition to the data in Figure 9 and Table 5, a ΔE_p (i.e., anodic peak potential minus cathodic peak potential) of 117 ± 18 mV is observed on average in Figure 6, which correlates closely to a two-electron exchange process (i.e., $\Delta E_p = 2.3RT/nF = 223$ mV/n at 1126 K).[37] As explained by Bard et al.[37]: "Even though the three possible rate-determining steps of the HER… are associated with the transfer of 1e, 1e, and 0e, respectively, each passage through the rate-determining step is proceeded or followed by one or two additional fast steps, such that two

electrons are always delivered." Hence, an *n*-value of 2 is consistent with a hydrogen evolution reaction (HER).

CV Analysis After $CaCl_2 \cdot 2H_2O$ Additions.—Two additions of $CaCl_2 \cdot 2H_2O$ were made while the $CaCl_2$ was molten to examine the effect of adding moisture to the electrochemistry. The resulting CV responses are shown in Figure 10. Peak B corresponds to the hypothesized hydrogen oxidation peak. As the amount of dihydrate introduced into the salt increased, the current in the vicinity of peaks B/B' increased. However, the baseline also shifted. Hence, an isolated analysis of peak B' is needed to deduce whether the added dihydrate increased oxidized species responsible for peak B'.

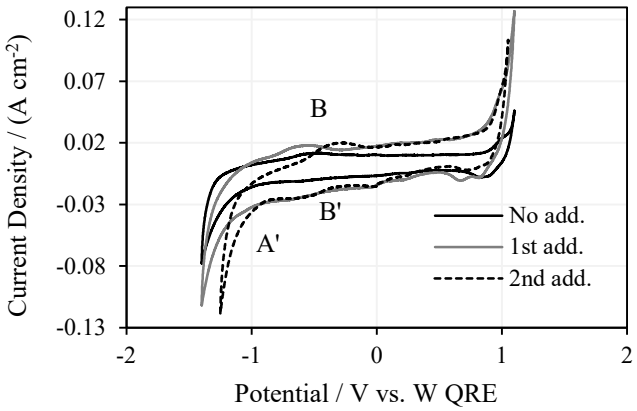

Figure 10. Cyclic voltammograms for experiment 5 with no, one, and two additions (add.) of $CaCl_2 \cdot 2H_2O$ at 700 mV s^{-1} (WE: 1.5 mm W rod, CE: 3.175 mm W rod, RE: 0.5 mm W wire).

Partial scans over peak B and B' were performed as shown in Figure 11. In the top plot, the baseline changed between the first and second additions. The background was removed in NOVA 2.1 and plotted to better compare B' peak sizes (Figure 11 bottom). Removing background makes it clearer that B' did indeed increase in size significantly from no dihydrate added, to the 1st addition, and slightly from the 1st addition to the 2nd addition. This is consistent

with Natsui et al.'s observation of the current increasing in this potential range with the addition of $CaCl_2 \cdot 2H_2O$.[9] This also aligns with the hypothesized identity of the peak, as the dihydrate will dissociate after entering the salt. The liberated water may dissociate (i.e., Eq. 5) or react to form HCl (i.e., $CaCl_2 + H_2O \leftrightarrow CaO + 2HCl$) to add H^+ ions to the system and increase the rate of the hydrogen redox reaction.

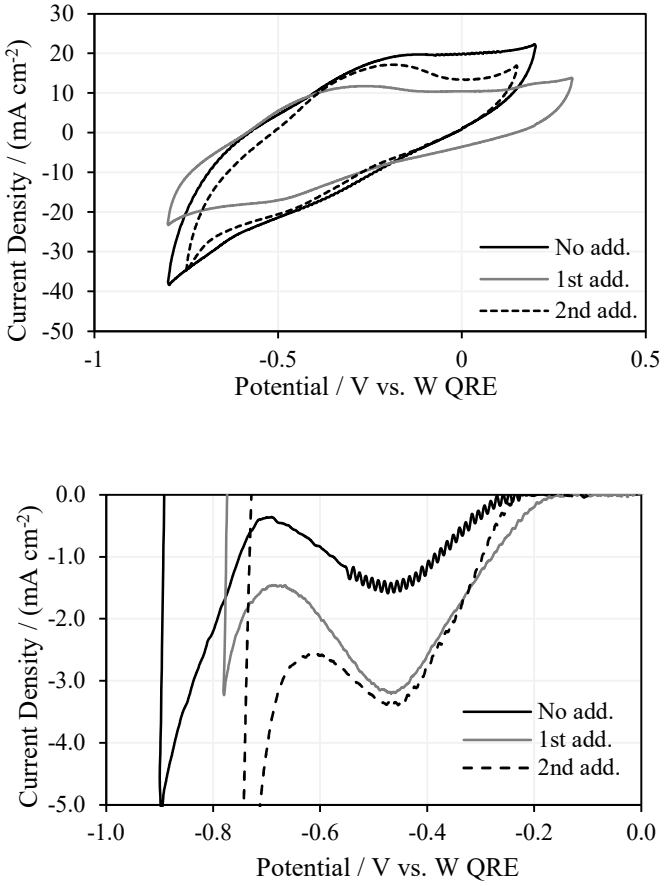

Figure 11. Overlaid CV responses for experiment 5 with no, one and two additions (add.) of $CaCl_2 \cdot 2H_2O$ at 700 mV s^{-1} without (top) and with (bottom) background subtracted (WE: 1.5 mm W rod, CE: 3.175 mm W rod, RE: 0.5 mm W wire).

Product Gas Analysis.—To verify the product of the electrochemical reaction corresponding to peak B', the same electrochemical cell (WE: W, CE: W, RE: W, $CaCl_2$ in

Al_2O_3 crucible) was set up in a sealed nickel chamber with an argon purge line and exhaust connected to a residual gas analyzer (see Gas Analyzer section). A linear sweep voltammogram (LSV) was performed to identify the location of the B' peak. The B' peak starts at about -0.5 V and peaks at about -0.75 V. In Figure 15, the electrolysis is started at 0 s of elapsed time. The signal intensity for 2 atomic mass units (AMU) molecules increased slightly above background levels after 40-60 seconds (lag time for the gas to accumulate, break the solubility limit, and reach the analyzer) when a potential of -0.5 V vs. W QRE was applied to the W WE and gas was produced. This rise in the 2 AMU signal was more significant at -0.8 and -0.9 V. A sharp drop in 2 AMU signal occurred for each applied potential shortly after terminating electrolysis. Due to the dilute nature of the hydrogen ions, only low gas production rates were possible, which led to only slightly above background levels detected at 2 AMU. The trend is more clearly seen when a moving 36-point average is calculated, as can be seen in Figure 12. This noticeable increase in intensity for 2 AMU provides further evidence that H_2 gas is a product of the electrochemical reaction associated with peak B'.

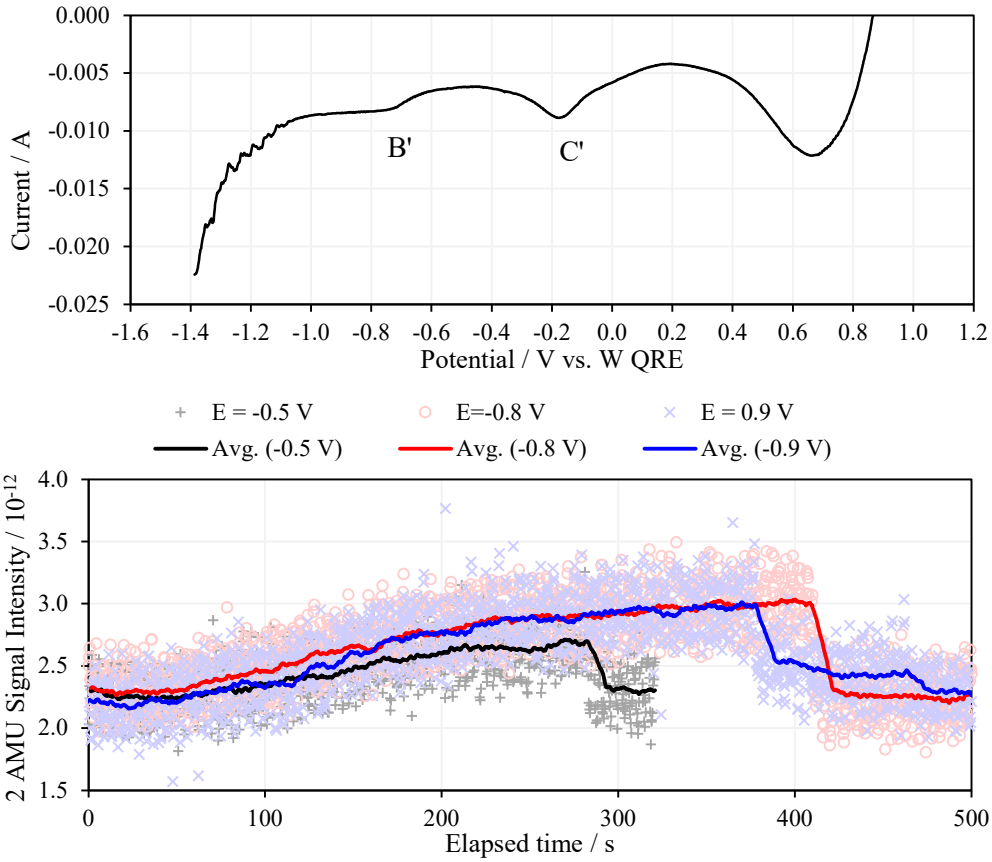

Figure 12. Top: Linear sweep voltammogram immediately prior to potential-controlled electrolysis (WE: 1.5 mm W rod, CE: 3.175 mm W rod, RE: 0.5 mm W wire) . Bottom: 2 AMU signal intensity (markers) vs. time for electrolysis applied at -0.5, -0.8, and -0.9 V with a 36-point moving average (lines) to highlight trend.

When the electrochemical reaction associated with peak B' occurs for a prolonged period during electrolysis, it is hypothesized that sufficient H_2 is accumulated near the WE surface to exceed the solubility of H_2 in molten $CaCl_2$. Bubbles begin to form and leave the salt. Hence, soluble-soluble behavior is observed in the relatively short measurements (i.e., on the order of 1 second) of CV, yet gas bubbles are formed when sufficient product is formed during prolonged electrolysis (i.e., on the order of 1 minute) (see discussion of Figure 8 in Cyclic Voltammetry section).

Concentration Estimate.—The concentration of the oxidized species for the B/B' redox couple in the molten salt can be estimated on an order of magnitude from the peak current (I_P) in CV measurements using the Randles-Ševčik equation:

$$I_P = -0.4463nFAC_{Ox}^{*}\sqrt{\frac{nFD_{Ox}\nu}{RT}} \quad (11)$$

where A is the WE area, C_{Ox}^{*} is the bulk concentration of the oxidized species, D_{Ox} is the diffusion coefficient of the oxidized species, and ν is the scan rate. A D_{Ox} value of 10^{-5} cm^2 s^{-1} was assumed for an order-of-magnitude concentration estimate because species in molten chloride salts often have a D_{Ox} close to or on the order of 10^{-5} cm^{-2} s^{-1}.[29,43,44] Using Eq. 11 with the slopes from Figure 7, calculations of the oxidized species in the B/B' redox couple concentration were performed, the results of which are displayed in Table 7. The molecular weight and a density of 2.05 g cm^{-3} for $CaCl_2$ were used to convert from molar concentration of the oxidized species to mole fraction in part-per-million (ppm).[45] If H^+ is assumed to be the oxidized species for the B/B' redox couple, then molar ppm in Table 7 converts to <1 ppm by weight. These concentration estimates indicate that CV can detect impurities at the ppm level and provide a rapid, *in situ* method to evaluate the purity and quality of the molten salts.

Table 7. Concentration estimates of H^+ in molten $CaCl_2$ using the slopes ($I_p A^{-1}\nu^{-1/2}$) from Figure 7.

Experiment No.	T / K	$I_p A^{-1}\nu^{-1/2}$ / (mA s$^{1/2}$ V$^{-1/2}$ cm^{-2})	C_{Ox} / (mol m^{-3})	C_{Ox} / ppm
1	1120	-1.4206	1.15	61.5
2	1131	-1.9199	1.56	83.5
3	1126	-1.8021	1.46	78.2
4	1123	-1.1628	0.94	50.4

Experiments 1 and 2 were handled according to the CEP method and experiment 3 and 4 were handled according to the DT method. The relatively small differences in the estimated oxidized species content of the salt appeared to indicate that 30 minutes of exposure of $CaCl_2$ within a container to low humidity air has a minimal impact on the amount of the hydrogen-containing impurity in the salt.

This analysis assumes a diffusion coefficient of 10^{-5} cm^2 s^{-1}, as discussed earlier. The diffusion coefficient of smaller ions, like H^+ and OH^- ions, may be higher than 10^{-5} cm^2 s^{-1}. Tritium ions ($^3H^+$) in LiF-BeF_2 has been calculated from 973 to 1373 K:[46]

$$D_{^3H^+}/(cm^2\ s^{-1}) = 2.758 \times 10^{-3} exp\left(-\frac{36.0\ kJ\ mol^{-1}}{RT}\right). \quad (12)$$

Using Eq. 12 to estimate the diffusion coefficient of H^+ (i.e., D_o), values from 5.8-6.0 × 10^{-5} cm^2 s^{-1} are calculated at 1120-1131 K (i.e., the temperature range of this study). Hence assuming a D_o of 10^{-5} cm^2 s^{-1} may result in an overestimate of the concentration of the oxidized species in the $CaCl_2$ bath.

Discussion

Possible Electrochemical Reactions.—For the B' signal, CV measurements suggest that two electrons are being exchanged and gas analyzer measurements indicate that a product of the reaction is H_2 gas. Using this information, some of the potential electrochemical reactions associated with the B' signal are listed below.

$$2H^+ + 2e^- \leftrightarrow H_2 \quad (6)$$

$$H_2O + 2e^- \leftrightarrow H_2 + O^{2-} \quad (13)$$

$$2H_2O + 2e^- \leftrightarrow H_2 + 2OH^- \quad (14)$$

$$2OH^- + 2e^- \leftrightarrow H_2 + 2O^{2-} \quad (15)$$

The existence of OH^- ion in molten $CaCl_2$ is conflicted in the literature. Zaikov et al.[47] state that "the hydroxide anions can exist as impurities in molten salts at temperatures above 1173 K (800 °C) [*sic*]" However, it is uncertain whether the authors intended 1073 K or 1173 K due to the conversion discrepancy. Regardless, the authors only state the possible existence of OH^- and provide no data nor references to support their statement. Mixtures of 20-30% $Ca(OH)_2$ and 70-80% $CaCl_2 \cdot 2H_2O$ were analyzed with thermogravimetric analysis (TGA) and X-ray diffraction (XRD) by Allal et al.[48] and evidence for CaOHCl was found at temperatures below ~773 K. Above ~773 K, Allal et al.[48] posit that CaOHCl decomposes to CaO, $CaCl_2$, and H_2O based on their TGA data, which supports the claim of CaOHCl dissociating at elevated temperature by Zaikov et al.[47] Faulkner et al.[22] performed TGA of 10% $Ca(OH)_2$ and 90% anhydrous $CaCl_2$ and observed a weight loss from 623 to 798 K, which coincided with the complete decomposition of $Ca(OH)_2$ to CaO. This temperature range agrees well with the thermal decomposition of pure $Ca(OH)_2$ observed by others.[23,24] Faulkner et al.[22] only observed the decomposition of $Ca(OH)_2$ step and no evidence of CaOHCl were observable in their TGA data. The data from the literature suggests that CaOHCl and $Ca(OH)_2$ both decompose to CaO above ~773 K.

Thermodynamic calculations were performed to estimate the concentrations of OH^- or $OHCl^{2-}$ at 1123 K. The Gibb's free energy change of reaction (ΔG_r^o) for the decomposition of $Ca(OH)_2$ (see Eq. 4) is -42.9 kJ/mol at 1123 K, which results in an equilibrium constant (K_{eq}) of 99.5 (i.e., $K_{eq} = exp(-\Delta G_r^o/RT)$).[49] As shown in Table 3, the concentration of O^{2-} was on the order of 100 ppm. The experiments were all conducted in a glovebox atmosphere where the H_2O was below 1 ppm. If the activity (a) of each species is assumed to be on the same order of

magnitude as their concentration, the concentration of OH^- is predicted to be one the order of 10^{-6} ppm (i.e., $a_{Ca(OH)_2} = a_{CaO}a_{H_2O}/K_{eq}$). A similar analysis using the thermodynamic data developed by Allal et al.[48] for the decomposition of CaOHCl and $Ca(OH)_2$ in the presences of $CaCl_2$ results in $OHCl^-$ and OH^- being on the order of 10^{-7} ppm. Hence, Eq. 14 and 15 appear to be unlikely based on the evidence in the literature.

In an attempt to differentiate Eq. 6 from 13, the theoretical standard redox potentials (E^o) were estimated relative to Cl^-/Cl_2 based on thermophysical properties from Barin[49] using the method presented by Zhang et al.[50] The calculated estimates of E^o are presented in the second column of Table 8. The estimated values of E^o were converted to AgCl(6 mol%)/Ag scale using the Nernst equation and assuming the activity of Ag, the reduced species (a_{red}), is unity and the activity of Ag^+, the oxidized species (a_{ox}), is equal to the mole fraction:

$$E_{eq} = E^o + \frac{RT}{nF}\ln\left(\frac{a_{ox}}{a_{red}}\right), \quad (16)$$

where E_{eq} is the equilibrium potential. The E^o for Eq. 13 is most closely correlated to peaks B'/B recalling from Figures 4-6 that peaks B'/B occur in the potential range of -0.45 to -0.95 V vs. Ag/AgCl (6 mol%). However, this does not consider the influence of activities. As estimated in Table 7, the mole fraction of the oxidized species could be as low as 5×10^{-5}. The O^{2-} content is on the order of 100 ppm by moles (see Table 3). If the activity of H_2 is assumed to be unity and the mole fraction is assumed to be equal to the activity of the oxidized species and the activity of O^{2-} for Eq. 13, the equilibrium potentials of Eq. 6 and 13 are calculated to be -0.459 V and -0.861 V vs. Ag/AgCl (6 mol%), respectively. The equilibrium potential of Eq. 6 is quite close to the beginning of peak B' (-0.45 V vs. Ag/AgCl (6 mol%), see Figures 4-6) and the equilibrium potential of Eq. 13 is near the tail for peak B' (-0.95 V vs. Ag/AgCl (6 mol%), see Figures 4-6).

Based on these thermodynamic calculations, Eq. 6 is the most probable reaction occurring for peaks B'/B. However, the oxidized species needs to be identified to conclusively determine the reaction occurring, which may require non-electrochemical measurements, such as optical spectroscopy measurements.

Table 8. Calculated estimates of E^o from thermophysical data for select redox reactions.

Redox Reaction	E^o / V vs. Cl^-/Cl_2	E^o / V vs. AgCl(6 mol%)/Ag
$2Cl^- + 2e^- \leftrightarrow Cl_2$	0.000	1.073
$Ag^+ + 1e^- \leftrightarrow Ag$	-0.801	0.272
$O_2 + 4e^- \leftrightarrow O^{2-}$	-0.844	0.229
$2H^+ + 2e^- \leftrightarrow H_2$	-1.053	0.202
$2OH^- + 2e^- \leftrightarrow H_2 + 2O^{2-}$	-1.580	-0.507
$H_2O + 2e^- \leftrightarrow H_2 + O^{2-}$	-1.807	-0.734

Challenges in Analysis.—Difficulties in identifying the oxidized species and estimating its concentration were the low signal-to-background ratio, the inability to make controlled additions of potential oxidized species, and no method available to the authors to quantify hydrogen in salt samples below 1 ppm. Because the peaks were small, the background was significant and needed to be subtracted. Attempts were made to consistently subtract the baseline by fitting a linear line in the -0.15 to -0.05 V vs. W QRE region. However, as seen in Figures 5 and 11, there is some variability in the baselines leading up to peaks. Hence, some adaptation of the potential range used for fitting the baseline was required but kept as minimal as possible. A calibration curve could not be developed using controlled additions of potential oxidized species because no stable source was identified at 1123 K. As shown in Figure 11, the amount of the oxidized species captured in the salt from similarly sized additions of $CaCl_2 \cdot 2H_2O$ was inconsistent between additions. $Ca(OH)_2$ could be used but decomposes to CaO and H_2O, which may also result in inconsistent uptake of the oxidized species into the salt. CaH_2 was tested, but

the hydrogen oxidation state of -1 yielded different electrochemical behavior. Lastly, attempts to use a Karl-Fisher titrator to quantify the hydrogen content in the salt were unsuccessful. There was no alternative method available to the authors to quantify hydrogen at less than 1 ppm by weight (110 ppm by moles) to verify the electrochemical concentration estimates. Hence, confirming the identity and more accurately quantifying the oxidized species is beyond the scope of this study and needs to be investigated in future studies.

Conclusions

Evidence suggests that the reduction peak occurring at around -0.5 V vs. W QRE (-0.9 V vs. Ag/AgCl[6 mol%]) corresponds to a two-electron exchange and produces H_2 gas. This evidence includes an increase in 2 AMU (H_2) signal measured with a gas analyzer when less than -0.5 V vs. W QRE is applied. Also, 2 electrons were estimated to be exchanged overall using soluble-soluble, reversible correlations for CV. A lack of dependence of peak potential on scan rate and linear trends between peak height and square root of scan rate for CV indicate that the reaction is reversible up to at least 1 V s^{-1}.

Adding $CaCl_2 \cdot 2H_2O$ increased the magnitude of peak B' linking H_2O as the direct (e.g., dissociation of water, reduction of water) or indirect (e.g., hydrolysis to form HCl) source of the oxidized species for the hydrogen gas evolution peak at -0.5 V vs W QRE. Thermodynamic calculations support H^+ as the oxidized species being reduced to H_2 gas. However, further evidence is needed to confirm H^+ as the oxidized species and its complexation with other species in the salt. The identification of the oxidized species and its structure would be a key point of investigation in future studies.

CV was used to estimate mole fractions of 5-10 × 10^{-5} for the oxidized species in electroreduction reaction producing hydrogen gas, which demonstrates the potential for electrochemical methods to detect trace impurities in molten salts. The different handling methods (CEP and DT) appeared to have minimal impact on the oxidized species concentration. Further studies involving the controlled addition or accurate quantification of potential oxidized species for the electrochemical reaction producing H_2 either *in situ* or *ex situ* would enable the identification of the oxidized species by confirming the similarity of the electrochemical response, the estimation of key properties (e.g., diffusion coefficient) and calibration of the measured peak current to the oxidized species content. The creation of a calibration curve will allow for the *in situ* measurement of the impurity within molten $CaCl_2$ down to the ppm level, which would enable rapid assessment of the quality of the salt for application in various technologies and chemical processes.

5. Acknowledgements

This work was supported by Battelle Savannah River Alliance, LLC under Contract No. 89303321CEM000080 with the U.S. Department of Energy.

References

1. T. Williams, R. Shum, and D. Rappleye, *J. Electrochem. Soc.*, **168**, 123510 (2021) https://doi.org/10.1149/1945-7111/ac436a.

2. T. Paget, J. A. McNeese, K. Fife, M. Jackson, and R. Watson, in *Plutonium Handbook*, D. L. Clark, Editor, vol. 1, American Nuclear Society, La Grange Park, IL (2019).

3. G. S. Perry and L. G. Macdonald, *J. Nucl. Mater.*, **130**, 234–241 (1985) http://www.sciencedirect.com/science/article/pii/0022311585903125.

4. K. S. Mohandas, *Miner. Process. Extr. Metall.*, **122**, 195–212 (2013) https://doi.org/10.1179/0371955313Z.00000000069.

5. A. M. Abdelkader, K. T. Kilby, A. Cox, and D. J. Fray, *Chem. Rev.*, **113**, 2863–2886 (2013) https://doi.org/10.1021/cr200305x.

6. K. Ono and R. O. Suzuki, *JOM*, **54**, 59–61 (2002) https://doi.org/10.1007/BF02701078.

7. G. Z. Chen, D. J. Fray, and T. W. Farthing, *Nature*, **407**, 361–364 (2000) https://www.nature.com/articles/35030069.

8. C. Peng, L. Chen, and M. Tang, *Fundam. Res.*, **2**, 578–587 (2022) https://www.sciencedirect.com/science/article/pii/S2667325821002612.

9. S. Natsui et al., *J. Sustain. Metall.*, **8**, 532–540 (2022) https://doi.org/10.1007/s40831-022-00516-w.

10. P. D. Myers and D. Y. Goswami, *Appl. Therm. Eng.*, **109**, 889–900 (2016) https://www.sciencedirect.com/science/article/pii/S1359431116311759.

11. W. Ding, A. Bonk, and T. Bauer, *Front. Chem. Sci. Eng.*, **12**, 564–576 (2018) https://doi.org/10.1007/s11705-018-1720-0.

12. B. Liu, X. Wei, W. Wang, J. Lu, and J. Ding, *Sol. Energy Mater. Sol. Cells*, **170**, 77–86 (2017) https://www.sciencedirect.com/science/article/pii/S0927024817302660.

13. G. Z. Chen and D. J. Fray, *J. Electrochem. Soc.*, **149**, E455 (2002) https://iopscience.iop.org/article/10.1149/1.1513985/meta.

14. H. Noguchi, S. Natsui, T. Kikuchi, and R. O. Suzuki, *Electrochemistry*, **86**, 82–87 (2018).

15. C. Zhang, D. Rappleye, A. Nelson, S. Simpson, and M. Simpson, *J. Electrochem. Soc.*, **168**, 097502 (2021) https://doi.org/10.1149/1945-7111/ac208e.

16. K. Dring, R. Dashwood, and D. Inman, *J. Electrochem. Soc.*, **152**, E104 (2005) https://iopscience.iop.org/article/10.1149/1.1860515/meta.

17. M. Mohamedi, B. Børresen, G. M. Haarberg, and R. Tunold, *J. Electrochem. Soc.*, **146**, 1472 (1999) https://iopscience.iop.org/article/10.1149/1.1391789/meta.

18. A. Mukherjee, R. Kumaresan, and S. Ghosh, *J. Electroanal. Chem.*, **902**, 115778 (2021) https://www.sciencedirect.com/science/article/pii/S1572665721008043.

19. M. Molenda, J. Stengler, M. Linder, and A. Wörner, *Thermochim. Acta*, **560**, 76–81 (2013) http://www.sciencedirect.com/science/article/pii/S0040603113001548.

20. H. U. Rammelberg, T. Schmidt, and W. Ruck, *Energy Procedia*, **30**, 362–369 (2012) https://www.sciencedirect.com/science/article/pii/S1876610212015597.

21. H. Kondo, Z. Asaki, and Y. Kondo, *Metall. Trans. B*, **9**, 477–483 (1978) https://doi.org/10.1007/BF02654424.

22. E. Faulkner, M. Monreal, M. Jackson, and M. F. Simpson, *J. Radioanal. Nucl. Chem.*, **326**, 1289–1298 (2020) https://doi.org/10.1007/s10967-020-07413-0.

23. P. E. Halstead and A. E. Moore, *J. Chem. Soc.*, 3873–3875 (1957) https://pubs.rsc.org/en/content/articlelanding/1957/jr/jr9570003873.

24. J. Yan and C. Y. Zhao, *Chem. Eng. Sci.*, **138**, 86–92 (2015) https://www.sciencedirect.com/science/article/pii/S0009250915005448.

25. R. Shibuya, S. Natsui, H. Nogami, T. Kikuchi, and R. O. Suzuki, *J. Electrochem. Soc.*, **167**, 102507 (2020) https://doi.org/10.1149/1945-7111/ab9961.

26. N. J. Gese and B. Pesic, in, TMS, San Antonio, TX (2013) https://inldigitallibrary.inl.gov/sites/sti/sti/5650454.pdf.

27. M. Gonzalez, A. Burak, S. Guo, and M. F. Simpson, *J. Nucl. Mater.*, **510**, 513–523 (2018) https://www.sciencedirect.com/science/article/pii/S0022311518304185.

28. Y. Kanzaki and M. Takahashi, *J. Electroanal. Chem. Interfacial Electrochem.*, **58**, 349–356 (1975) https://www.sciencedirect.com/science/article/pii/S0022072875800921.

29. M. Schvaneveldt, R. Fuller, and D. Rappleye, *J. Electroanal. Chem.*, **918**, 116442 (2022) https://doi.org/10.1016/j.jelechem.2022.116442.

30. M. Schvaneveldt, thesis, Brigham Young University, Provo, UT (2022) https://scholarsarchive.byu.edu/etd/9707.

31. J. A. H. Oates, *Lime and Limestone*, John Wiley & Sons, Ltd, (1998) https://doi.org/10.1002/9783527612024.

32. G. Moe, Ed., *Alloy Selection for Service in Chlorine Hydrogen Chloride and Hydrochloric Acid - A Guide to the Use of Nickel-Containing Alloys (3rd Edition)*, Nickel Institute, (2022) https://nickelinstitute.org/media/8da1c603db456db/hydrochloricacid-hydrogenchloride-chlorine_10020.pdf.

33. Y. Ihara, H. Ohgame, K. Sakiyama, and K. Hashimoto, *Corros. Sci.*, **22**, 901–912 (1982) https://www.sciencedirect.com/science/article/pii/0010938X82900609.

34. K. Dring, R. Bhagat, M. Jackson, R. Dashwood, and D. Inman, *J. Alloys Compd.*, **419**, 103–109 (2006) http://www.sciencedirect.com/science/article/pii/S0925838805015227.

35. J. E. B. Randles, *Trans. Faraday Soc.*, **44**, 327–338 (1948) https://pubs.rsc.org/en/content/articlelanding/1948/tf/tf9484400327.

36. R. S. Nicholson and Irving. Shain, *Anal. Chem.*, **36**, 706–723 (1964) https://doi.org/10.1021/ac60210a007.

37. A. J. Bard, L. R. Faulkner, and H. S. White, *Electrochemical Methods: Fundamentals and Applications*, 3rd ed., p. 1104, John Wiley & Sons, Inc., Hoboken, NJ, (2022).

38. T. Berzins and P. Delahay, *J. Am. Chem. Soc.*, **75**, 555–559 (1953) http://dx.doi.org/10.1021/ja01099a013.

39. X. Zhao, H. Ren, and L. Luo, *Langmuir*, **35**, 5392–5408 (2019) https://doi.org/10.1021/acs.langmuir.9b00119.

40. F. Lantelme, H. Alexopoulos, and O. Haas, *J. Appl. Electrochem.*, **19**, 649–656 (1989) https://doi.org/10.1007/BF01320639.

41. In *Solubility Data Series*,, vol. 45/46, Pergamon Press, New York (1991).

42. Y. Zeng et al., *Nucl. Eng. Technol.*, **51**, 490–494 (2019) https://www.sciencedirect.com/science/article/pii/S1738573318301967.

43. J. Zhang, *J. Nucl. Mater.*, **447**, 271–284 (2014) http://www.sciencedirect.com/science/article/pii/S0022311513013032.

44. G. J. Janz and N. P. Bansal, *J. Phys. Chem. Ref. Data*, **11**, 505–693 (1982) https://doi.org/10.1063/1.555665.

45. G. J. Janz et al., *J. Phys. Chem. Ref. Data*, **4**, 871–1178 (1975) http://aip.scitation.org/doi/10.1063/1.555527.

46. S. T. Lam et al., *J. Mater. Chem. A*, **9**, 1784–1794 (2021) https://pubs.rsc.org/en/content/articlelanding/2021/ta/d0ta10576g.

47. Y. P. Zaikov, V. P. Batukhtin, N. I. Shurov, L. E. Ivanovskii, and A. V. Suzdaltsev, *Metall. Mater. Trans. B*, **45**, 961–967 (2014) https://doi.org/10.1007/s11663-013-9990-x.

48. K. M. Allal, J. C. Dolignier, and G. Martin, *Rev. Inst. Fr. Pétrole*, **52**, 361–368 (1997) https://ogst.ifpenergiesnouvelles.fr/articles/ogst/abs/1997/03/allal_v52n3/allal_v52n3.html.

49. I. Barin, *Thermochemical Data of Pure Substances*, 3rd ed., VCH Verlagsgesellschaft mbH., Weinheim, (1995).

50. W. Zhang, C. R. Pulham, A. R. Mount, N. Brockie, and R. Lewin, *Energy Mater.*, **3**, 132–136 (2008) https://doi.org/10.1179/174892408X394254.